Article

Recurrent interactions in local cortical circuits

Simon Peron[1,4 ✉], Ravi Pancholi[2], Bettina Voelcker[2], Jason D. Wittenbach[1], H. Freyja Ólafsdóttir[1,3,5], Jeremy Freeman[1] & Karel Svoboda[1]

Most cortical synapses are local and excitatory. Local recurrent circuits could implement amplification, allowing pattern completion and other computations[1–4]. Cortical circuits contain subnetworks that consist of neurons with similar receptive fields and increased connectivity relative to the network average[5,6]. Cortical neurons that encode different types of information are spatially intermingled and distributed over large brain volumes[5–7], and this complexity has hindered attempts to probe the function of these subnetworks by perturbing them individually[8]. Here we use computational modelling, optical recordings and manipulations to probe the function of recurrent coupling in layer 2/3 of the mouse vibrissal somatosensory cortex during active tactile discrimination. A neural circuit model of layer 2/3 revealed that recurrent excitation enhances sensory signals by amplification, but only for subnetworks with increased connectivity. Model networks with high amplification were sensitive to damage: loss of a few members of the subnetwork degraded stimulus encoding. We tested this prediction by mapping neuronal selectivity[7] and photoablating[9,10] neurons with specific selectivity. Ablation of a small proportion of layer 2/3 neurons (10–20, less than 5% of the total) representing touch markedly reduced responses in the spared touch representation, but not in other representations. Ablations most strongly affected neurons with stimulus responses that were similar to those of the ablated population, which is also consistent with network models. Recurrence among cortical neurons with similar selectivity therefore drives input-specific amplification during behaviour.

Two circuit motifs contribute to neural dynamics in cortical layer 2/3 (L2/3): recurrent excitation, which may cause amplification[1–5,11,12], and feedback inhibition, which may account for the sparse activity typical of L2/3[12–14]. We explored the role of these motifs in an integrate-and-fire model of L2/3 of the mouse vibrissal somatosensory ('barrel') cortex constrained by measured physiological properties[15,16] (Methods).

To model input-specific recurrent coupling, we restricted the sensory input to a subnetwork of the excitatory neurons (200 out of 1,700), corresponding to the number of L2/3 barrel cortex neurons that respond to active touch[7,17] (Fig. 1a). We simulated touch-related input to L2/3 based on recordings of their L4 inputs[18] (Methods). To measure how accurately neural activity reflects the sensory input, we computed an 'encoding score' ($R_{stimulus}$) by cross-correlating the spike rate of each neuron with the input (Methods).

We varied recurrence by changing the connection probability within the input-recipient subnetwork (subnetwork connectivity; synaptic conductance was scaled proportionately[5]) (Methods). For the connectivity of each subnetwork, we matched the distribution of the encoding score to that measured in vivo[7] by adjusting the strength of the L4 input. Subnetworks with connectivity equal to and moderately increased

relative to the rest of the network (non-subnetwork connectivity, 0.2; subnetwork connectivity range, 0.2–0.4) produced responses that were consistent with those observed in vivo[7] (Fig. 1b, Methods). The strength of sensory input required to match in vivo responses declined with increasing subnetwork connectivity. Amplification—defined as the ratio of network output to network input—therefore increased with subnetwork connectivity[1] (Fig. 1c). Additional increases in subnetwork connectivity (>0.4) produced all-or-none network responses, in which a transient input drove the network into a persistently active state[19] (Extended Data Fig. 1).

Overall, subnetwork behaviour fell into three regimes, each of which produced a distinct response to removal (or ablation) of a small number of neurons. Subnetworks with low connectivity (0.2) amplified little, and were resistant to ablation (Fig. 1c–f). Encoding scores for spared neurons increased after simulated ablation of 10% of the subnetwork[14], owing to reduced feedback inhibition[13,20] (encoding score, from 0.237 ± 0.027 to 0.274 ± 0.032 (grand median $\pm$ adjusted median absolute deviation (MAD)); $P < 0.001$, Wilcoxon signed-rank test, across $n = 30$ simulated networks with different randomized connectivity and initial conditions) (Fig. 1d–f, Methods).

[1]Janelia Research Campus, Howard Hughes Medical Institute, Ashburn, VA, USA. [2]Center for Neural Science, New York University, New York, NY, USA. [3]Department of Cell and Developmental Biology, University College London, London, UK. [4]Present address: Center for Neural Science, New York University, New York, NY, USA. [5]Present address: Donders Institute for Brain Cognition and Behaviour, Radboud University, Nijmegen, The Netherlands. ✉e-mail: speron@nyu.edu
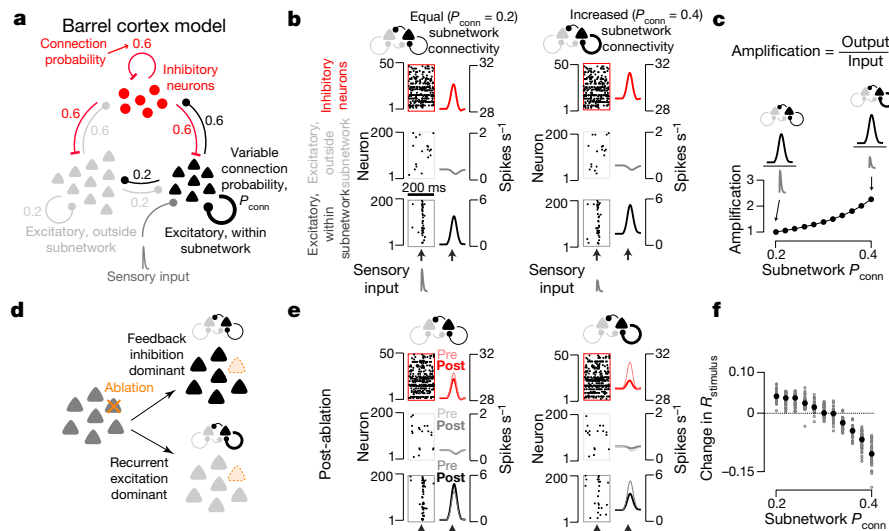
Fig. 1 | Ablation effect in simulated cortical L2/3 network depends on excitatory connectivity. a, The L2/3 network model comprises a subnetwork of 200 excitatory neurons (black) receiving sensory input (dark grey), a larger excitatory population (1,500 neurons; light grey) without sensory input, and 300 inhibitory neurons (red). All populations are interconnected (connection probabilities listed in figure) (Methods). The probability and strength of connections within the excitatory subnetwork was varied (P_{conn}, thick black loop) (Methods). **b**, Model network responses aligned to input (arrows). Left, subnetwork connectivity for excitatory subnetwork equal to overall connection probability. Right, increased connectivity. Raster plots show a subset of neurons from an example network. Peri-stimulus time histograms (PSTHs) show mean values across all neurons and networks ($n = 30$). Bottom, excitatory neurons within subnetwork; middle, excitatory neurons outside subnetwork; top, inhibitory neurons. **c**, Amplification, defined as the ratio of network output to sensory input (Methods), as a function of subnetwork connectivity, normalized to $P_{conn} = 0.2$ (mean across 30 networks per P_{conn}). **d**, Predicted effects of ablation. In the equal-connectivity case (top), feedback inhibition dominates and responses among spared neurons increase. In the increased-connectivity case (bottom), recurrent excitation dominates and responses decline. **e**, As in **b**, but after ablation of the 20 neurons with the strongest encoding score. **f**, Effect of ablation on stimulus encoding, as a function of subnetwork connectivity. Grey points denote cross-neuron median for individual network. Black circles denote the grand median of 30 simulated networks.

Subnetworks with increased connectivity (for example, 0.4) exhibited stronger amplification[1,4] (Fig. 1c). Ablations reduced encoding scores for spared neurons, from 0.243 ± 0.049 to 0.143 ± 0.028 (connectivity = 0.4; $P < 0.001$, $n = 30$ networks), because of reduced amplification (Fig. 1d–f). Networks in the all-or-none regime[19] were robust to ablation, and maintained their all-or-none response (Extended Data Fig. 1). The response of subnetworks to ablations therefore distinguishes the three regimes.

We next performed a similar analysis for actual L2/3 networks during behaviour. We trained mice with a single spared whisker on an object localization task (Fig. 2a, b, Methods) and recorded neural activity with volumetric imaging[7] in L2/3 of the barrel column corresponding to the spared whisker ($8,126 \pm 2,436$ (mean ± s.d.) neurons per mouse, $n = 16$ mice) (Fig. 2c, Extended Data Table 1, Methods). Activity in a subset of neurons encoded whisker position (hereafter whisking neurons), whereas others responded to touch-induced changes in whisker curvature (hereafter touch neurons)[7] (Fig. 2d, e). An encoding model generated a prediction of neural activity from vibrissal kinematics (Methods). Correlating the prediction with the actual neural activity yielded an encoding score, which was used to assign neurons to the touch and/or the whisking representations[7] (Methods). Across 16 mice (Extended Data Table 1), 901 ± 539 of the imaged neurons encoded touch (fraction: 0.108 ± 0.051) and 865 ± 364 encoded whisking (fraction: 0.106 ± 0.028).

We probed the roles of recurrence by ablating members of the touch representation and examining the effect on spared neurons. Several excitatory neurons were ablated using multiphoton excitation[9,10] (Extended Data Figs. 2, 3). Ablating a small proportion of strong touch cells (16.8 ± 12.8 neurons, 6% of touch neurons in the barrel column of the spared whisker, $n = 9$ mice; touch score, 70th ± 35th percentile) (Fig. 2f) reduced responses to touch in the spared touch neurons (Fig. 2g, h). The touch-encoding score (R_{touch}) across touch neurons declined (from 0.123 ± 0.021 to 0.100 ± 0.037 (grand median ± adjusted MAD); $n = 9$ mice, 8,392 neurons, $P = 0.004$, Wilcoxon signed-rank test

for mouse medians, paired by mouse) (Fig. 2j, Methods), as did the touch neuron count (from 932 ± 634 to 716 ± 469 (mean ± s.d.), calculations exclude ablated neurons) (Methods). The whisking-encoding score ($R_{whisking}$) did not change (from 0.116 ± 0.013 to 0.115 ± 0.024; 6,975 neurons, $P = 0.820$; neuron count: from 775 ± 267 to 721 ± 241) (Fig. 2i, k).

In the model, more extensive ablations caused larger declines in encoding scores (Extended Data Fig. 4). In agreement with this prediction, the decline in touch representation increased as more of the touch representation was ablated (Pearson correlation of change in R_{touch} and net R_{touch} ablated, $R = -0.794$, $P < 0.001$ across all 24 ablations; $R = -0.779$, $P = 0.013$ for the 9 touch cell ablations) (Fig. 2l). Touch neurons proximal (15–35 μm) to the ablated cells experienced a larger decline in R_{touch} values than those distal (115–135 μm) from the ablated cells (Fig. 2m). The effects of ablating the touch neurons decayed over a distance ($\lambda = 87$ μm, exponential fit) (Fig. 2m) similar to the spatial scale of local recurrent connectivity in the rodent sensory cortex[21]. Whisking neurons exhibited no distance-dependent changes (Extended Data Fig. 5). The declining touch representation was not caused by changes in whisker movement or behaviour (Extended Data Fig. 6). This result is consistent with amplification of touch responses by recurrent excitation in L2/3.

By contrast, ablating a subset of strong whisking neurons (12.7 ± 5.7 neurons, approximately 4% of whisking neurons in the barrel column of the spared whisker, $n = 7$ mice; whisking score: 66th ± 37th percentile) produced no effect on either the touch representation (R_{touch} from 0.112 ± 0.081 to 0.095 ± 0.069, $n = 7$ mice, 5,866 neurons; $P = 0.109$, count from 838 ± 401 to 899 ± 548) or the whisking representation ($R_{whisking}$ from 0.108 ± 0.076 to 0.107 ± 0.076, $n = 6,161$; $P = 0.812$, count from 880 ± 387 to 974 ± 558) (Fig. 2j, Extended Data Fig. 7). Similarly, ablating silent neurons (event rate below 0.025 Hz; 16.3 ± 2.6 neurons, $n = 8$ mice) did not change the touch representation (R_{touch} from 0.115 ± 0.021 to 0.107 ± 0.023, $n = 8$ mice, 7,110 neurons; $P = 0.383$, count from 889 ± 713 to 926 ± 681) (Fig. 2k, Extended Data Fig. 7, Methods) or the whisking representation ($R_{whisking}$ from 0.115 ± 0.014 to 0.114 ± 0.015, 7,684 neurons; $P = 0.844$, count from
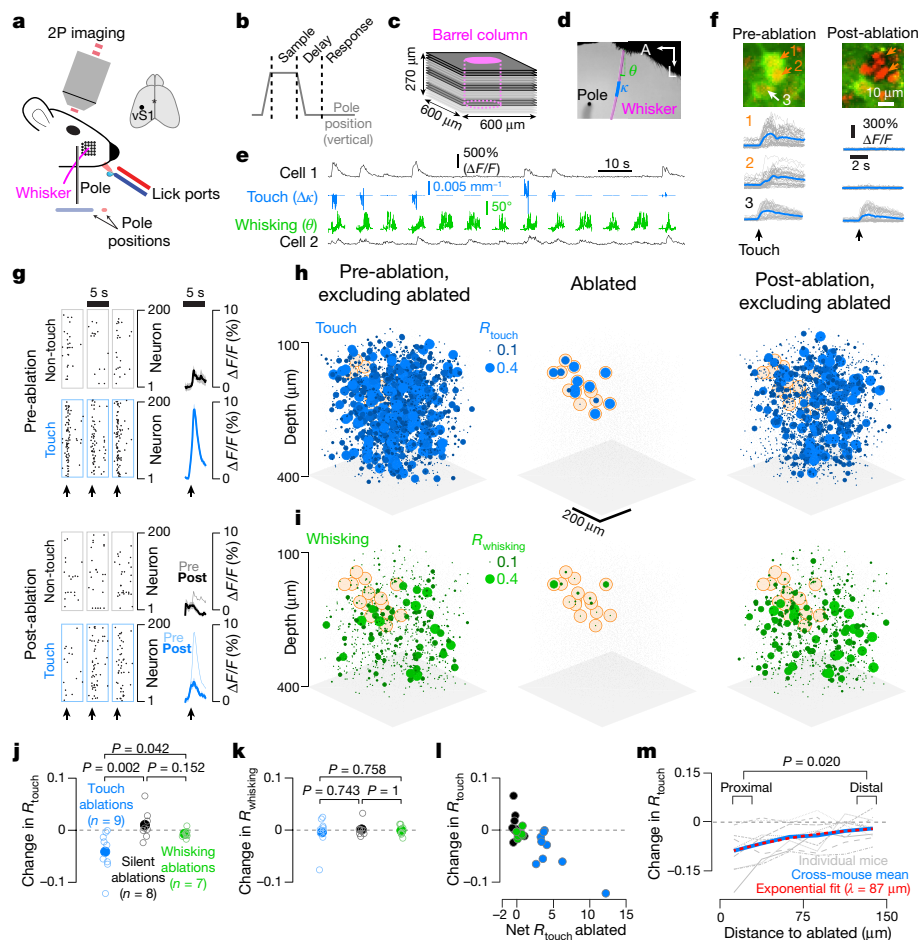
Fig. 2 | Touch networks of the barrel cortex are sensitive to ablation. a, Mice used one whisker to locate a pole and reported the perceived position by licking one of two lick ports (red or blue). **b**, Task epochs (Methods). **c**, Imaging planes were centred on the barrel column of the spared whisker (magenta). Three planes were imaged simultaneously (same shade of grey). **d**, Example video frame showing the whisker (magenta), pole (black), whisker curvature (κ, blue), and whisker angle (θ, green). **e**, Neuronal activity for a touch (cell 1) and whisking (cell 2) cell. Blue denotes change in whisker curvature ($\Delta\kappa$); green denotes whisker angle (θ). **f**, Ablations. Pyramidal neurons 1 and 2 (orange) were ablated (green, GCaMP6s; red, mCherry). Bottom, touch-aligned neuronal responses. **g**–**i**, Example experiment. **g**, Touch responses (dots, calcium events) (Methods) for a subset of neurons before (top) and after (bottom) ablation. Grey boxes denote 200 non-touch, non-whisking neurons; blue boxes denote 200 touch neurons. Right, touch-aligned mean $\Delta F/F$ values across these neurons for the strongest 5% of touches. Shading denotes s.e.m. **h**, Left, map for touch cells before ablation. Sphere size denotes R_{touch} values. Grey dots denote other neurons. Orange denotes the position of ablated neuron. Centre, R_{touch} values for ablated neurons. Right, R_{touch} values after ablation. **i**, As in **h**, but for whisking neurons. **j**, Median change in R_{touch} values across neurons in individual mice after ablation. Blue, touch ablations; black, silent neuron ablations; green, whisking ablations. P values determined by Wilcoxon rank-sum test. **k**, As in **j**, but for $R_{whisking}$ values. **l**, Ablation effect on change in R_{touch} value as a function of R_{touch} values summed over the ablated neurons. Colour as in **j**. **m**, Distance-dependence (with respect to closest ablated neuron) of change in R_{touch} after ablation. Proximal change in P_{touch}: −0.132 ± 0.246 (grand median ± adjusted MAD), distal: −0.056 ± 0.241; P value determined by Wilcoxon signed-rank test for proximal versus distal medians, paired by mouse, n = 9 mice.

961 ± 464 to 904 ± 384). Touch ablations produced significantly different changes in encoding scores among touch (but not whisking) representations than either whisking or silent ablations, whereas whisking ablations did not produce significantly different changes from silent ablations (Fig. 2j, k). Non-specific effects of ablation therefore do not contribute to changes in the touch representation after ablation.

Ablation of whisking neurons did not degrade the whisking representation. Our network model suggests that the slower kinetics of the whisking input do not account for this lack of effect, as networks having increased subnetwork connectivity (0.4) with slower input (t_{peak} = 50 ms, versus 10 ms for touch simulations) were sensitive to simulated ablation (Extended Data Fig. 8, Methods). Touch input is in-phase across the neural population[17,18], which engages recurrent excitation. By contrast, individual neurons encode whisking input with different phases[22]; this asynchronous population response is expected to engage recurrent excitation less effectively. Therefore, the lack of sensitivity to ablation in the whisking population does not necessarily indicate an absence of recurrent coupling.

In recurrent networks connected in a feature-specific manner[5], the effects of ablation on spared neurons should increase with the similarity of their tuning to the ablated population[23,24]. We tested this intuition in our model, defining the response similarity as the correlation of single neuron activity with the mean activity of the ablated neurons (Fig. 3a, Methods). In networks with increased subnetwork connectivity, neurons with high response similarity showed the largest decline in encoding score after ablation (Fig. 3b). In networks without increased subnetwork connectivity, the relationship disappeared (Fig. 3b).

We performed a similar analysis on our experimental data. Because not all neurons were recorded simultaneously (Fig. 2c, Methods), it was not possible to compute a mean across ablated neurons or correlations between that mean and the activity of individual neurons. We therefore devised a response similarity metric that did not require simultaneous recording. For each neuron, we averaged pre-ablation responses across both trial types (Fig. 3c). Concatenating these yielded the trial-averaged $\Delta F/F$ of the neuron (Fig. 3d). Computing the mean trial-averaged $\Delta F/F$ across all ablated neurons provided the ablated
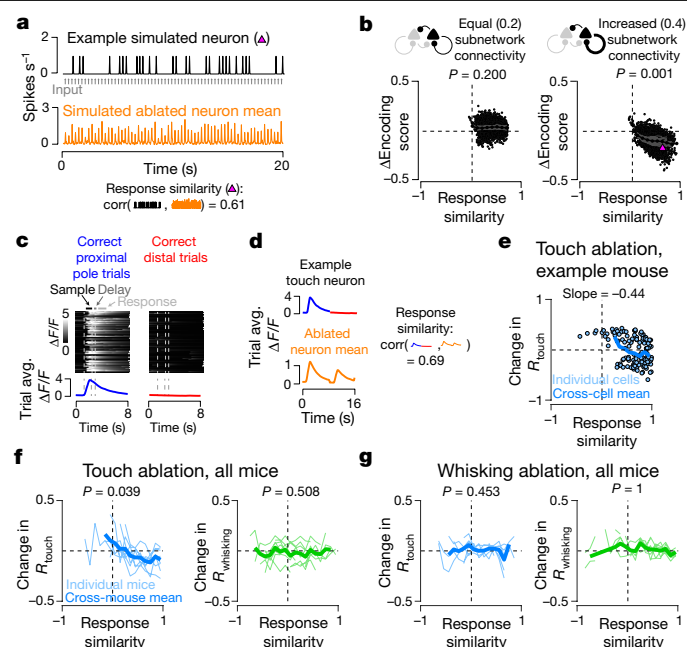
Fig. 3 | Effect of ablations depends on response similarity to ablated cells. a, Response similarity in simulated networks. Top, example neuron spike rate (black). Grey arrows denote sensory input. Orange denotes mean spike rate across ablated neurons. Bottom, response similarity was computed by correlating neuronal spike rate with the mean ablated neuron spike rate. **b**, Dependence of the change in encoding score after ablation on response similarity in model networks. Grey dots denote individual neurons. Dark grey lines denote single network averages. P values for sign test that the slopes of linear fits across all networks ($n = 30$; $P_{conn} = 0.2$ case: 3,779 neurons; $P_{conn} = 0.4$ case: 3,466 neurons) are 0. Black line denotes grand mean across networks. Magenta triangle denotes neuron from **a**. **c**, Trial averaged response for example touch neuron. Heat maps show $\Delta F/F$ values for individual trials (proximal pole trials, left; distal, right). Bottom, trial-averaged $\Delta F/F$ values. **d**, Top, trial-averaged $\Delta F/F$ values for neuron in **c**. Bottom, the mean trial-averaged response across ablated neurons. Right, response similarity is the correlation of individual neuron trial-averaged response vectors with the mean across ablated neurons. **e**, Changes induced by ablation of touch neurons on the touch score as a function of response similarity in an example mouse. Blue circles denote individual neurons; blue line denotes binned mean (Methods). Slope for a linear fit of the points is given. **f**, Population data for all touch ablations for both touch (blue, left) and whisking (right, green) neurons. Thin coloured lines denote individual mouse mean values for a given response similarity bin; thick lines denote cross-mouse mean values. P values are from a sign test in which the slope of change in encoding score as a function of response similarity is 0 ($n = 9$ mice; 2,768 touch neurons; 1,085 whisking neurons). **g**, As in **f**, but for ablation of whisking neurons ($n = 7$ mice; 1,692 touch neurons; 935 whisking neurons).

neuron mean response. Response similarity was measured for each neuron as the correlation between its trial-averaged $\Delta F/F$ response and the mean response across all ablated neurons.

Changes in R_{touch} values after ablation depended on response similarity (Fig. 3e, f). R_{touch} values in neurons with high response similarity declined. Neurons with negative response similarity showed increased R_{touch} values, potentially owing to reduced feedback inhibition previously evoked by the ablated neurons[20] (Fig. 3e). Ablation of touch neurons had no effect on the whisking network (Fig. 3f). Ablation of whisker neurons had no effect on either representation (Fig. 3g).

Targeted photoablation allowed us to test the roles of recurrence in cortical circuits[1]. The selective degradation of representations similar to the ablated neurons is consistent with amplification in recurrent networks[1–4,11,12,23–26] (Fig. 1), but inconsistent with circuit models of sparse coding that are dominated by feedback inhibition[12,14,20,27] or

models with all-or-none activity[19]. Our experiments reveal that cortical circuits can be surprisingly sensitive to damage targeting specific representations, despite remarkable robustness to other types of perturbation[28].

Online content

Any methods, additional references, Nature Research reporting summaries, source data, extended data, supplementary information, acknowledgements, peer review information; details of author contributions and competing interests; and statements of data and code availability are available at https://doi.org/10.1038/s41586-020-2062-x.

1. Douglas, R. J., Koch, C., Mahowald, M., Martin, K. A. & Suarez, H. H. Recurrent excitation in neocortical circuits. *Science* **269**, 981–985 (1995).
2. Chance, F. S., Nelson, S. B. & Abbott, L. F. Complex cells as cortically amplified simple cells. *Nat. Neurosci.* **2**, 277–282 (1999).
3. Christie, I. K., Miller, P. & Van Hooser, S. D. Cortical amplification models of experience-dependent development of selective columns and response sparsification. *J. Neurophysiol.* **118**, 874–893 (2017).
4. Miller, K. D. Canonical computations of cerebral cortex. *Curr. Opin. Neurobiol.* **37**, 75–84 (2016).
5. Cossell, L. et al. Functional organization of excitatory synaptic strength in primary visual cortex. *Nature* **518**, 399–403 (2015).
6. Lee, W. C. et al. Anatomy and function of an excitatory network in the visual cortex. *Nature* **532**, 370–374 (2016).
7. Peron, S. P., Freeman, J., Iyer, V., Guo, C. & Svoboda, K. A cellular resolution map of barrel cortex activity during tactile behavior. *Neuron* **86**, 783–799 (2015).
8. Peron, S. & Svoboda, K. From cudgel to scalpel: toward precise neural control with optogenetics. *Nat. Methods* **8**, 30–34 (2011).
9. König, K., Becker, T. W., Fischer, P., Riemann, I. & Halbhuber, K. J. Pulse-length dependence of cellular response to intense near-infrared laser pulses in multiphoton microscopes. *Opt. Lett.* **24**, 113–115 (1999).
10. Vladimirov, N. et al. Brain-wide circuit interrogation at the cellular level guided by online analysis of neuronal function. *Nat. Methods* **15**, 1117–1125 (2018).
11. Rubin, D. B., Van Hooser, S. D. & Miller, K. D. The stabilized supralinear network: a unifying circuit motif underlying multi-input integration in sensory cortex. *Neuron* **85**, 402–417 (2015).
12. Harris, K. D. & Mrsic-Flogel, T. D. Cortical connectivity and sensory coding. *Nature* **503**, 51–58 (2013).
13. Mateo, C. et al. In vivo optogenetic stimulation of neocortical excitatory neurons drives brain-state-dependent inhibition. *Curr. Biol.* **21**, 1593–1602 (2011).
14. Barrett, D. G., Denève, S. & Machens, C. K. Optimal compensation for neuron loss. *eLife* **5**, e12454 (2016).
15. Avermann, M., Tomm, C., Mateo, C., Gerstner, W. & Petersen, C. C. Microcircuits of excitatory and inhibitory neurons in layer 2/3 of mouse barrel cortex. *J. Neurophysiol.* **107**, 3116–3134 (2012).
16. Lefort, S., Tomm, C., Floyd Sarria, J. C. & Petersen, C. C. The excitatory neuronal network of the C2 barrel column in mouse primary somatosensory cortex. *Neuron* **61**, 301–316 (2009).
17. Crochet, S., Poulet, J. F., Kremer, Y. & Petersen, C. C. Synaptic mechanisms underlying sparse coding of active touch. *Neuron* **69**, 1160–1175 (2011).
18. Hires, S. A., Gutnisky, D. A., Yu, J., O'Connor, D. H. & Svoboda, K. Low-noise encoding of active touch by layer 4 in the somatosensory cortex. *eLife* **4**, (2015). https://doi.org/10.7554/eLife.06619
19. Litwin-Kumar, A. & Doiron, B. Slow dynamics and high variability in balanced cortical networks with clustered connections. *Nat. Neurosci.* **15**, 1498–1505 (2012).
20. Chettih, S. N. & Harvey, C. D. Single-neuron perturbations reveal feature-specific competition in V1. *Nature* **567**, 334–340 (2019).
21. Holmgren, C., Harkany, T., Svennenfors, B. & Zilberter, Y. Pyramidal cell communication within local networks in layer 2/3 of rat neocortex. *J. Physiol. (Lond.)* **551**, 139–153 (2003).
22. Curtis, J. C. & Kleinfeld, D. Phase-to-rate transformations encode touch in cortical neurons of a scanning sensorimotor system. *Nat. Neurosci.* **12**, 492–501 (2009).
23. Marshel, J. H. et al. Cortical layer-specific critical dynamics triggering perception. *Science* **365**, eaaw5202 (2019).
24. Carrillo-Reid, L., Han, S., Yang, W., Akrouh, A. & Yuste, R. Controlling visually guided behavior by holographic recalling of cortical ensembles. *Cell* **178**, 447–457 (2019).
25. Lien, A. D. & Scanziani, M. Tuned thalamic excitation is amplified by visual cortical circuits. *Nat. Neurosci.* **16**, 1315–1323 (2013).
26. Daie, K., Svoboda, K. & Druckmann, S. Targeted photostimulation uncovers circuit motifs supporting short-term memory. Preprint at https://www.bioRxiv.org/content/10.1101/623785v1 (2019).
27. Hansel, D. & van Vreeswijk, C. The mechanism of orientation selectivity in primary visual cortex without a functional map. *J. Neurosci.* **32**, 4049–4064 (2012).
28. Li, N., Daie, K., Svoboda, K. & Druckmann, S. Robust neuronal dynamics in premotor cortex during motor planning. *Nature* **532**, 459–464 (2016).

Article

Methods

Network model

We modelled the L2/3 network associated with a single barrel column—one of the most extensively studied cortical microcircuits[29,30]—as a network of leaky integrate-and-fire neurons[31]. The dynamics of each neuron were governed by:

$$\tau \frac{dV_i}{dt} = V_r - V(t) + R[I_i^{exc}(t) + I_i^{inh}(t) + I_i^{ext}(t)] \quad (1)$$

where V is the membrane potential, V_r is the rest/reset potential, τ is the membrane time constant, R is the input resistance, I^{exc} and I^{inh} are excitatory and inhibitory synaptic currents, I^{ext} is a current representing sensory stimulus drive (for example, from layer 4 inputs), and i indexes the neurons in the network. When the membrane potential reaches the spiking threshold, V_{th}, a spike is emitted, the membrane potential is reset to V_r, and the dynamics of the neuron are frozen for a short refractory period, t_{ref}. The synaptic currents follow kick-and-decay dynamics:

$$\tau_{syn} \frac{dI_i^{syn}}{dt} = -I_i^{syn} + \tau_{syn} \sum_{j,k} w_{ij}\delta(t - t_i^{syn} - t_d) \quad (2)$$

where 'syn' denotes the type of synapse (either excitatory or inhibitor), τ_{syn} is the synaptic time constant, w_{ij} is a matrix of synaptic strengths from neuron j to neuron i, t_{jk} is the time of the kth spike of neuron j, and t_d is the spike transmission delay. The sum over j is over all neurons, while the sum over k is over all spikes from that neuron.

The network comprised 2,000 neurons, of which 1,700 (85%) were excitatory and 300 (15%) were inhibitory[16]. Excitatory neurons had $\tau = 30$ ms, whereas inhibitory neurons had faster dynamics with $\tau = 10$ ms[15,16]. As the subthreshold dynamics for these neurons are linear, the behaviour of these neurons is invariant to changes of scale in V. The meaningful quantity is $\Delta V = V_{th} - V_r$, which we assume to be, on average, 35 mV for all neurons[15,16]. Each neuron was assigned a value chosen uniformly within a range of ±50% of this mean value. Excitatory and inhibitory post-synaptic currents had time constants of $\tau_{exc} = 2$ ms and $\tau_{inh} = 3$ ms, respectively. The refractory period for spiking was $t_{ref} = 0.5$ ms. Synapses had a mean synaptic delay of $t_d = 0.6$ ms[15]; each individual synapse was assigned a value chosen within a range of ±50% of this mean value. Although all neural parameters could be modelled as random variables, we found that jittering ΔV for the neurons and t_d for the synapses provided sufficient heterogeneity to give a broad range of baseline spike rates across neurons and also prevented network synchronization. The input resistance, R, was factored into the synaptic weights and the magnitudes of the external currents, as described below.

The excitatory population was subdivided into two groups: a small input-recipient subnetwork of 200 neurons and the remainder of the excitatory population (1,500 neurons). Although all neurons in L2/3 probably receive touch-related input from L4[32], only a small proportion are driven to spike after touch[7,17], justifying this model assumption. We neglected feedforward inhibition[33]. This is justified because feedforward inhibition simply rescales input from L4[2], which in our model is adjusted to produce experimental observed population activity levels. Thus, each neuron belonged to one of three groups: the excitatory subnetwork (S), the remainder of the excitatory population (E), or the inhibitory population (I). Connections between neurons are determined by a block stochastic model. Given two neurons—the first from group A, the second from group B—there was a fixed probability of a connection from the first neuron to the second, denoted p_{AB}.

In our 'equal subnetwork connectivity' network, we used sparse connectivity between excitatory neurons, $p_{SS} = p_{SE} = p_{ES} = p_{EE} = 0.2$, and more dense connectivity both within the inhibitory population as well as between the excitatory and inhibitory populations, $p_{II} = p_{IS} = p_{IE} = p_{SI} = p_{EI} = 0.6$ (refs. [15,16]). All connections had the same strength, which was chosen so that the resulting post-synaptic potential (PSP) is 1 mV (refs. [15,16]). Because it is the only connectivity parameter that was varied systematically, we denote p_{SS} as 'P_{conn}' in the rest of the text.

In the increased-subnetwork-connectivity version of the network, P_{conn} was increased to 0.4. To replicate the experimentally observed relationship between connectivity and synaptic strength[5], the synaptic weight for these connections was increased to give PSPs of 1.6 mV. Networks with other levels of connectivity within the subnetwork were produced by linear interpolation or extrapolation of both P_{conn} and synaptic strength between the equal-subnetwork-connectivity and increased-subnetwork-connectivity cases.

The stimulus drive to the network was modelled as an external current targeting the excitatory subnetwork (group S; $I^{ext} = 0$ for all neurons in groups E and I). For each stimulus presentation, the waveform of the current was modelled with a beta distribution with shape parameters $\alpha = 3$ and $\beta = 5$. The beta distribution is defined on the interval [0, 1], giving a distinct beginning and end to the stimulus. For the chosen shape parameters, the beta distribution has a value of 0 at its end points and a peak at $(\alpha - 1)/(\alpha + \beta - 2)$. To model the fast touch stimulus, the waveform was stretched in time so that the peak occurs 10 ms after the start (full-width half-maximum, 12.8 ms)[18]. The amplitude of the stimulus waveform was chosen so that the network response matched the experimental data. All neurons also receive tonic background input in the form of a Poisson spike train of excitatory spikes with a frequency of 5,000 Hz for excitatory neurons and 2,000 Hz for inhibitory neurons; these values were selected so that the tonic firing rate of these populations were approximately 0.5 Hz for excitatory neurons and 10 Hz for inhibitory neurons[34–36].

Simulations were performed in Python using the Brian2 simulation package[37] with a step-size of $dt = 0.1$ ms. For each randomly sampled network connectivity, the network was first simulated for 20 s of model time (corresponding to 66 stimulus presentations) and spike trains for all neurons were recorded. The activity of each neuron was then given an encoding score, which quantifies the signal-to-noise ratio of the representation of the stimulus: the spike train of the neuron was convolved with a Gaussian kernel (standard deviation, 20 ms) to produce a firing rate; the firing rate as well as the stimulus waveform was down-sampled by a factor of 5 (to a sample period of 0.5 ms) and the normalized cross-correlation between the signals was computed for leads/lags up to 10 ms; the peak value this cross-correlation is the encoding score.

We first ran exploratory simulations to constrain the strength of the input to the subnetwork to match physiological data[7]. We simulated both the equal-subnetwork-connectivity ($P_{conn} = 0.2$) and the increased-subnetwork-connectivity ($P_{conn} = 0.4$) networks across a range on sensory input strengths. In both cases, we examined the distributions of excitatory neuron encoding scores as a function of input strengths, selecting the input strength that produced a distribution most closely matching the experimental data (in terms of distribution shape and fraction of neurons encoding the stimulus). With input strengths defined for these two cases, we then used linear interpolation or extrapolation to select the input strength for other amounts of subnetwork connectivity. Because this procedure ensured a fixed network output following the simulated sensory stimulus, amplification (ratio of network output to sensory input) (Fig. 1c) was defined as the inverse of the sensory input strength[2]. Amplification was normalized to the case where neurons within the input-recipient subnetwork had connectivity probabilities equal to the non-input recipient excitatory population (that is, $P_{conn} = 0.2$).

The final set of simulations explored the effects of targeted ablation across a range of subnetwork connectivity levels (Figs. 1, 3, Extended Data Fig. 1), number of ablations (Extended Data Fig. 4), and input kinetics (Extended Data Fig. 8). To simulate targeted ablation, we used

30 randomized network instances for each subnetwork connectivity level, number of ablations, and input rise time, and calculated the pre-ablation encoding score for each neuron. The 20 excitatory neurons with the highest encoding score were then removed (all outgoing synaptic strengths set to 0), the simulation was repeated, and the encoding scores after ablation were computed. Examination of the effects of the number of ablated neurons was done with the top 0, 10, 20, 50 and 100 neurons (Extended Data Fig. 4). This was repeated for 30 different realizations of the stochastic network connectivity. Neurons were considered to be part of the sensory input representation if they had an encoding score above 0.1; the effect of the ablation (Fig. 1e, f) was quantified as the change in encoding score across all neurons that met the 0.1 encoding score criteria either before and/or after ablations. The response similarity analysis (Fig. 3) used a more stringent encoding score cut off of 0.25; using a cut off of 0.1 did not alter the result, but reduced the magnitude of the observed effect. The ablated neurons were excluded for calculations of the distributions encoding scores before and after ablation, as well as in constructing PSTHs (Fig. 1b, e).

In modelling the effect of the number of neurons ablated on the change in encoding score (Extended Data Fig. 4), we restricted our modelling to the increased subnetwork connectivity case, $P_{conn} = 0.4$. For simulations of 'whisking' input (Extended Data Fig. 8), we shifted from a 'touch'-like stimulus, peaking 10 ms after stimulus onset, to one peaking 50 ms after onset to mimic the response to whisking input observed in vivo[17,18,22,35]. We examined both the equal ($P_{conn} = 0.2$) and increased ($P_{conn} = 0.4$) connectivity cases.

For large subnetwork connectivity ($P_{conn} > 0.4$), the network transitioned to all-or-none behaviour, where strong enough input can drive the subnetwork into a state of persistent increased firing[19] (Extended Data Fig. 1). To reset the network after such a transition, we introduced a strong pulse of excitatory current to the inhibitory population 300 ms after the stimulus onset. In this regime, the extrapolation scheme for setting the stimulus strength did not apply, because spike rate was dictated by network properties and not the input strength. Instead, the input strength affected the reliability with which a stimulus would cause a transition to the state of increased firing. We found that choosing a stimulus strength that was twice that dictated by our extrapolation scheme produced a reasonable number of stimulus-encoding neurons. Thus, we used this criterion to set the input strength in this regime.

PSTHs were constructed by averaging the Gaussian-convolved (kernel standard deviation, 20 ms) responses of individual neurons, aligned to the sensory input.

Determining model synaptic weights

Model synapses were defined by kick-and-decay dynamics of the post-synaptic currents. We set the synaptic weights to produce a desired amplitude of the resulting unitary PSP. Here, we derive the relationship between the synaptic weight and the PSP size that allows us to do this.

Assume that a synaptic current starts at $I = 0$ when a single spike of weight w arrives at $t = 0$. In the absence of any other spikes, the subsequent time-course of the current is found by integrating equation (2):

$$I(t) = we^{-t/\tau_{syn}} \tag{3}$$

To determine the resulting behaviour of $V(t)$, make the assumption that the PSP evolves according to a difference of exponentials:

$$V(t) = V_0(e^{-t/\tau_1} - e^{-t/\tau_2}) \tag{4}$$

Differentiating equation (4) and using equation (3), one can show that this form does indeed solve equation (3) if we choose:

$$\tau_1 = \tau_m, \ \tau_2 = \tau_{syn}, \text{ and } V_0 = \frac{Rw}{\tau_m/\tau_s - 1} \tag{5}$$

The PSP size is the maximum value of $V(t)$, which we can compute as:

$$V_{max} = V_0 a^{(1-a^{-1})^{-1}}(a - 1) \tag{6}$$

in which $a = \tau_m/\tau_s$ is the ratio of the time constants. Comparing this to the expression for V_0 in equation (6) we find our desired relationship:

$$Rw = V_{max} a^{(1-a^{-1})^{-1}} \tag{7}$$

The linearity of the synaptic dynamics allows us to use equation (7) to avoid explicitly determining the value of R.

Mice

All procedures were performed in compliance with the Janelia Research Campus Institutional Animal Care and Use Committee and the New York University University Animal Welfare Committee. Two transgenic lines were used for these experiments, differentiated in Extended Data Table 1 by a 'j' or 'n' in mouse ID. Mice with IDs starting with letter 'j' consisted of mice expressing nuclear localized mCherry in a Cre-dependent manner (R26-LSL-H2B-mCherry[7]; JAX 023139) crossed with mice expressing Cre in cortical pyramidal neurons (Emx1-IRES-cre[38]; JAX 005628). In cortical L2/3, these mice expressed nuclear mCherry only in nuclei of excitatory neurons. Several (9 or 12) injections (450 μm deep, 300 μm apart; beveled pipettes, World Precision Instruments; 20 nl each, at 10 nl min^{−1} with a custom-built microinjector) of AAV2/1-syn-GCaMP6s (UPenn AV-1-PV2824)[39] were made in barrel cortex (3.6 mm lateral, 1.5 mm posterior) of young adult mice[7] (6–8 week). After viral injection, a titanium head bar was attached to the skull and the craniotomy was covered with a cranial window. Craniotomies were always over the left hemisphere. Mice with IDs starting with 'n' consisted of mice expressing GCaMP6s in a Cre-dependent manner (Ai162[40], JAX 031562), crossed with Slc17a7-IRES2-cre[40] (JAX 023527) to restrict expression to in pyramidal neurons. Surgeries for these mice did not include viral injections but were otherwise identical. With the exception of j258836, all mice were male.

Behaviour

Approximately one week after surgery, mice were trimmed to a single row of whiskers (typically the C row) and placed on water restriction[41] (1 ml per day). Training commenced 5–7 days after restriction onset. Mice were trained on an object-localization task[42,43] (Fig. 2a, b). If the pole appeared in a range of proximal positions, the mouse would be rewarded with a small water drop for licking the right lick port; pole presentation at the distal position would be rewarded upon licking the left lick port (Fig. 2a). Trials consisted of a 1–1.2-s sample epoch followed by a 0.5–1.2-s delay epoch after which a 50- or 100-ms 3.4 kHz auditory response cue signalled to the mouse to respond (Fig. 2b). To prevent premature licking, the lick port was brought into tongue range by a motor (Zaber) only during the response epoch (Fig. 2b). Mice exhibiting excessive premature licking (licks before reward cue on >20% of trials; licks monitored with a laser beam; Thorlabs) were not used.

Mice were trimmed to a single whisker after reaching criterion performance ($d' > 1.5$ for two consecutive days). The spared whisker barrel column was identified using the neuropil signal, as described previously[7]. Whisker videography was performed at 400–500 Hz. Whiskers were tracked using an automated software pipeline[44] and then curated using custom browser software[7].

Mice were assigned randomly to experimental groups (ablation type). Experimenters were not blinded to the group.

Imaging

Calcium imaging was performed using a custom two-photon microscope (http://openwiki.janelia.org/wiki/display/shareddesigns/MIMMS) with a 16×, 0.8 NA objective (Nikon)[7]. GCaMP (BG22; Chroma) and mCherry (675/70 filter; Chroma) fluorescence was imaged using

Article

GaAsP PMTs (Hamamatsu). The 940 or 1,000 nm (Coherent) imaging beam was steered with a 16 kHz line rate resonant galvanometer (Thorlabs); a piezo collar (Physik Instrumente) moved the focus axially. The 512 × 512 pixel images were collected at 7 Hz, with three 600 × 600-µm images per piezo cycle. Planes were spaced 15 µm apart. Scanimage[45] (Vidrio Technologies, http://www.vidriotech.com) controlled the microscope. Three planes, constituting a 'subvolume', were imaged simultaneously (4–6 subvolumes, spanning 45 µm each, 12–18 total planes, 180–270 µm in depth total), and power was modulated with depth using a length constant of 250 µm. Deeper subvolumes were typically imaged with higher power, using a similar length constant. Individual subvolumes were typically imaged for 50 trials per day, with all subvolumes usually visited on any given day. Alignment across days was performed as previously described[7,46].

Imaging data were processed using a semi-automated software pipeline that included image registration, segmentation, neuropil subtraction, $\Delta F/F$ computation, and event detection[7]. The de-noised $\Delta F/F$ trace, which consisted of the event amplitude trace convolved with event-specific exponential rise and decay, was used for analysis.

Neuronal classification

Neurons were classified using a linear-nonlinear encoding model[7,47]. The model consisted of a cascaded generalized linear model that used a temporal and stimulus domain kernel to predict the activity of individual neurons given whisker angle, θ, or whisker curvature, κ, assuming Gaussian noise with input nonlinearities.

The model predicted the neuronal response, r (that is, $\Delta F/F$), as

$$r \sim \text{Norm}(z, \sigma^2)$$

$$z = f_1(s_1) \times k_1 + f_2(s_2) \times k_2$$

Here, s_1 and s_2 are the whisker angle, θ, and whisker curvature, κ, respectively. The terms f_1 and f_2 are static, point-wise nonlinearities comprising a weighted sum of 16 triangular basis functions

$$f = \sum_{i=1}^{16} w_i b_i(x)$$

in which x is the input (s_1 or s_2), with each b_i given by

$$b_i = \begin{cases} (x - x_{i-1})/(x_i - x_{i-1}), i > 1, x_{i-1} < x < x_i \\ (x_{i+1} - x)/(x_{i+1} - x_i), i < N, x_i \le x < x_{i+1} \\ 0, \text{otherwise} \end{cases}$$

k_1 and k_2 are temporal kernels consisting of 14 time points (2 s).

Thus, the model gives a z-scored prediction of neural activity, z, by fitting parameters k_1, k_2, f_1 and f_2 for given whisker kinematic parameters, s_1 and s_2.

The model parameters k_1, k_2, f_1 and f_2 were fit using maximum likelihood with block coordinate descent. This procedure reliably estimated model parameters within three to five iterations.

To avoid degeneracy associated with arbitrary scaling factors on either the kernels or the nonlinearities, the nonlinearities were forced to have minimum of 0 and maximum of 1. Temporal kernels were unconstrained.

A prior was used to ensure smoothness of both the temporal kernels and the nonlinearities and prevent over-fitting. Specifically, the prior added a factor to the objective function penalizing excessive second derivatives of the temporal kernels and nonlinearities. Employing such a prior corresponds to maximizing the log-posterior, with the prior adding a small penalty to the objective function. To fit several thousand cells efficiently, the scale factor associated with this penalty was determined from a cross-validated inspection of a random subset of neurons.

The model was fit using fivefold cross-validation across trials. That is, a randomly selected 80% of trials were used for fitting, and 20% were used for evaluation, with 5 distinct evaluation groups per fit ensuring all data was used for fitting in exactly one case. The Pearson correlation between the predicted and actual $\Delta F/F$ yielded a measure of the quality of the model fit. This correlation was used as the encoding score for barrel cortex data: R_{touch}, based on $\Delta \kappa$ for touch, and $R_{whisking}$, based on whisker θ for whisking (Fig. 2d, e). A neuron was considered part of a representation if R_{touch} or $R_{whisking}$ exceeded 0.1 and if the neuron score was above the 99th percentile of scores measured from matched shuffled neural activity. These criteria are more stringent than those used previously[7], because ablation predominantly impacted neurons with high encoding scores. Using a less stringent criterion did not change the underlying conclusions, but did dilute the magnitude of the effect. For the response similarity analysis (Fig. 3), a threshold of 0.25 was used for the encoding score.

Shuffled activity was generated by randomizing the timing of the calcium events to construct a novel de-noised $\Delta F/F$ trace. Matched shuffled activity was selected by using neurons from the same imaging subvolume (that is, concurrently imaged to ensure identical mouse behaviour) sharing a similar event rate. Event rates were matched by partitioning the neurons from a subvolume into 10 equally sized bins (in terms of neuron count). Thus, in addition to the aforementioned encoding score threshold, a given neuron R value had to exceed the 99th percentile of R values obtained across neurons in the same subvolume and event rate bin whose event times were shuffled.

We examined robustness by partitioning individual days into two interdigitated pseudo-sessions, and measuring the correlation between encoding scores for the two pseudo-sessions[7]. The resulting correlations ranged between approximately 0.5 and 0.75. Neural classification (whisking and touch) was stable across days for trained mice. Furthermore, the touch neuron curvature kernels assumed 'V'- or 'L'-like shapes[7], meaning that high magnitude curvature changes drove the largest responses, a result consistent with the known responses of these neurons. Finally, the kernels were stable across days[7]. Thus, changes in barrel cortex encoding after ablation are not a reflection of the variability inherent to the encoding model, but rather reflect genuine changes in the underlying representations.

Ablated neurons were always excluded from analysis of experimental data, including calculations of pre-ablation population encoding scores. Analyses involving data before and after ablation were pooled across several behavioural sessions. Pre- and post-ablation data each consisted of at least two (but typically three) behavioural sessions, with each subvolume sampled on most sessions. Given that a single subvolume was imaged for around 50 trials in a session, classification typically used around 150 behavioural trials per neuron (minimum for encoding model: 100 trials). Neurons participating in both representations in a given area were excluded from analysis. In all cases in which comparisons of pre- and post-ablation distributions were made, neurons were included for analysis if they met the criteria for representation membership (described above) in the pre- or post-ablation period, or during both periods.

Multiphoton ablation

Ablations[9,48,49] were performed with 880 nm (Chameleon Ultra 2; Coherent) or 1,040 nm (Fidelity HP; Coherent) femtosecond laser pulses delivered through a 0.8 NA, 16× objective (Nikon) in mice that were awake but not performing the task or lightly anesthetized using isoflurane (1–2%). On the day of ablation, a new image was acquired and a warp field transform was used to find the target neurons[46]. Imaging was not performed on the day of ablation; post-ablation analyses used the imaging data from the 2–4 behavioural sessions on the days after ablation. Typically, experiments consisted of three days of pre-ablation data collection, the ablation day, and three days of post-ablation data collection.

In virally transfected mice, the mCherry signal was used to restrict ablations to pyramidal neurons[7]; in mice endogenously expressing GCaMP, presence of fluorophore was used for this purpose. The neurons with strongest touch or whisking encoding scores within the spared barrel column were targeted for ablation. The percentage of touch and whisking neurons ablated was calculated in relation to the estimated 1,691 pyramidal neurons in L2/3[16], of which 17% (287) belonged to each representation[7]. Neurons participating in both representations (touch and whisking) were avoided. For silent cell ablation, neurons with a calcium event rate below 0.025 Hz were targeted for ablation.

In all cases, approximately 2/3 of ablations were successful (Extended Data Fig. 2c). Proximity to vasculature, low baseline fluorescence, and excessive depth accounted for most failures. Thus, despite targeting the strongest neurons in a given representation, the actual representation strength of ablated neurons varied. The encoding score percentile of the ablated neurons is therefore reported in the text.

After ablation we consistently observed an increase in GCaMP6 fluorescence in the targeted neuron (Extended Data Fig. 2a, b). Taking advantage of this signature, the ablation protocol consisted of interleaved 'ablation' and 'evaluation' epochs (ablation duration: 50–200 ms; evaluation: 0.1–2 s, with longer evaluation times proving more reliable) (Extended Data Fig. 2b). Ablation epoch power started at the evaluation epoch power (25–100 mW, measured at the specimen) and rose linearly as necessary (up to 1 W) over the course of several seconds. The beam was focused on the brightest part of the targeted neuron using a pair of galvanometers (Cambridge Technology) and oscillated over a path spanning 1–2 µm. Evaluation epoch fluorescence data were collected using standard resonant galvanometer imaging[7], although restricted to a single plane (approximately 30 Hz). Ablations were terminated after observation of the fluorescence rise in the target neuron.

Consistent with similar protocols[10,50], ablation did not produce off-target damage: calcium event rates for neurons adjacent (10–25 µm) to ablated cells did not change after the ablation of silent neurons (Extended Data Fig. 3a), and glial immunoreactivity was confined to the site of the lesioned neuron (Extended Data Fig. 3b–d).

Typically, 10–50 ablations were performed over the course of one hour. For histological analysis (Extended Data Fig. 3b–d), perfusion was performed 24 h after ablation in two *Emx1-IRES-cre × LSL-H2B-mCherry* mice (9 and 28 ablations were successful in these mice, approximating typical experimental conditions). Alternating cryomicrotome (Leica) sections were exposed to antibodies for either the microglial marker IBA1 (Abcam, ab5076) or the astrocytic marker GFAP (Abcam, ab7260). Glial reactions were measured by first locating the centre of the ablated neuron in the glial immunoreaction image. An edge detection algorithm[39] that operated on an intensity image in angle-distance space from the neuron centre detected the extent of the reaction (Extended Data Fig. 3d). Specifically, intensity profiles were measured across a range of angles emanating from the point within the ablation. To delimit the glial reaction, large drops in intensity were detected. Glia was considered reactive if the intensity inside the detected reaction area was two standard deviations above background image intensity.

Following ablation, nearby neurons retained sensory responses (Fig. 2f), event rate (Extended Data Fig. 3a), and maintained structural integrity (Extended Data Fig. 3b, c, e). In a few instances ($n = 5$) the ablation termination protocol failed, resulting in more extensive lesions (Extended Data Fig. 3f). These experiments were excluded from the study.

We excluded ablated neurons as well as neurons within a cylinder centred on ablated neurons having a radius of 10 µm and a height of 60 µm from all analyses. This excluded neurons abutting ablated cells, and ensured no neurons within a typical glial reaction radius would be included.

Response similarity

For simulated data, response similarity was measured by taking the Pearson correlation of the Gaussian-convolved (kernel standard deviation, 20 ms) activity of an individual neuron with the mean Gaussian-convolved activity of the ablated neurons (Fig. 3a). For experimental data, response similarity was measured by correlating the individual neuronal trial averaged $\Delta F/F$ to the ablated neuron trial average mean. For each neuron, trial averaged $\Delta F/F$ was calculated by taking the mean $\Delta F/F$ across all correct proximal and distal pole trials (Fig. 3c), then concatenating these two vectors (Fig. 3d). The mean of these vectors across the ablated neurons constituted the ablated neuron mean (Fig. 3d). Response similarity is simply the Pearson correlation of the individual neuron trial averaged $\Delta F/F$ with the mean trial averaged $\Delta F/F$ across all ablated neurons. Single-network (Fig. 3b) or mouse (Fig. 3e–g) averages were computed with response similarity bins having a width of 0.1. The grand mean of these is shown as a dark line on these plots. Only strongly responding neurons (encoding score > 0.25) were considered in this analysis (other analyses use a cut-off value of 0.1).

Trial-averaged $\Delta F/F$ correlations were used instead of raw activity correlations because neurons were not all imaged simultaneously; only neurons in a given subvolume were imaged simultaneously. Because ablated neurons came from multiple subvolumes, response similarity had to use trial-averaged responses to allow for comparison across disjointly recorded populations.

Statistical analyses

Most statistical comparisons were performed using the Wilcoxon signed-rank test comparing paired medians within individual mice for two conditions (for example, before and after ablation, or proximal and distal encoding score change). For cases in which values had no natural pairing (comparison of different ablation types), the Wilcoxon rank-sum test comparing medians was used to compare distributions. To test whether encoding score change depended on response similarity (Fig. 3), we first fit a line to individual networks or mice (for example, Fig. 3e; the linear fit is distinct from the cross-cell mean that is shown). Next, we tested whether the slopes thus obtained were distinct from 0 across all networks or mice using the non-parametric sign test.

In all cases, we used the median of single-neuron values within a mouse. That is, we treated mice, and never neurons, as independent observations. Where relevant, the total number of neurons included across all mice was given. Where given, adjusted MAD was calculated by multiplying the median absolute deviation by 1.4826 so as to approximate the standard deviation under conditions of normality. Sample sizes were similar to those used by others in the field. No statistical tests were used to determine sample sizes.

Reporting summary

Further information on research design is available in the Nature Research Reporting Summary linked to this paper.

Data availability

Data can be found at CRCNS (http://crcns.org/) at https://doi.org/10.6080/K0Z31WWG.

Code availability

Code for the simulations can be found at https://github.com/jwittenbach/ablation-sim. Code used for data analysis can be found at https://github.com/peronlab/ablation.

29. Petersen, C. C. & Crochet, S. Synaptic computation and sensory processing in neocortical layer 2/3. *Neuron* **78**, 28–48 (2013).
30. Petersen, C. C. H. Sensorimotor processing in the rodent barrel cortex. *Nat. Rev. Neurosci.* **20**, 533–546 (2019).

Article

31. Brette, R. et al. Simulation of networks of spiking neurons: a review of tools and strategies. *J. Comput. Neurosci.* **23**, 349–398 (2007).
32. Bureau, I., von Saint Paul, F. & Svoboda, K. Interdigitated paralemniscal and lemniscal pathways in the mouse barrel cortex. *PLoS Biol.* **4**, e382 (2006).
33. Xue, M., Atallah, B. V. & Scanziani, M. Equalizing excitation-inhibition ratios across visual cortical neurons. *Nature* **511**, 596–600 (2014).
34. Gentet, L. J. et al. Unique functional properties of somatostatin-expressing GABAergic neurons in mouse barrel cortex. *Nat. Neurosci.* **15**, 607–612 (2012).
35. Yu, J., Gutnisky, D. A., Hires, S. A. & Svoboda, K. Layer 4 fast-spiking interneurons filter thalamocortical signals during active somatosensation. *Nat. Neurosci.* **19**, 1647–1657 (2016).
36. Yu, J., Hu, H., Agmon, A. & Svoboda, K. Recruitment of GABAergic interneurons in the barrel cortex during active tactile behavior. *Neuron* **104**, 412–427 (2019).
37. Stimberg, M., Brette, R. & Goodman, D. F. Brian 2, an intuitive and efficient neural simulator. *eLife* **8**, e47314 (2019).
38. Gorski, J. A. et al. Cortical excitatory neurons and glia, but not GABAergic neurons, are produced in the Emx1-expressing lineage. *J. Neurosci.* **22**, 6309–6314 (2002).
39. Chen, T. W. et al. Ultrasensitive fluorescent proteins for imaging neuronal activity. *Nature* **499**, 295–300 (2013).
40. Daigle, T. L. et al. A suite of transgenic driver and reporter mouse lines with enhanced brain-cell-type targeting and functionality. *Cell* **174**, 465–480 (2018).
41. Guo, Z. V. et al. Procedures for behavioral experiments in head-fixed mice. *PLoS ONE* **9**, e88678 (2014).
42. O'Connor, D. H. et al. Vibrissa-based object localization in head-fixed mice. *J. Neurosci.* **30**, 1947–1967 (2010).
43. Guo, Z. V. et al. Flow of cortical activity underlying a tactile decision in mice. *Neuron* **81**, 179–194 (2014).
44. Clack, N. G. et al. Automated tracking of whiskers in videos of head fixed rodents. *PLoS Comput. Biol.* **8**, e1002591 (2012).
45. Pologruto, T. A., Sabatini, B. L. & Svoboda, K. ScanImage: flexible software for operating laser scanning microscopes. *Biomed. Eng. Online* **2**, 13 (2003).
46. Huber, D. et al. Multiple dynamic representations in the motor cortex during sensorimotor learning. *Nature* **484**, 473–478 (2012).
47. Ahrens, M. B., Paninski, L. & Sahani, M. Inferring input nonlinearities in neural encoding models. *Network* **19**, 35–67 (2008).
48. Orger, M. B., Kampff, A. R., Severi, K. E., Bollmann, J. H. & Engert, F. Control of visually guided behavior by distinct populations of spinal projection neurons. *Nat. Neurosci.* **11**, 327–333 (2008).
49. Allegra Mascaro, A. L., Sacconi, L. & Pavone, F. S. Multi-photon nanosurgery in live brain. *Front. Neuroenergetics* **2**, 21 (2010).
50. Canty, A. J. et al. In-vivo single neuron axotomy triggers axon regeneration to restore synaptic density in specific cortical circuits. *Nat. Commun.* **4**, 2038 (2013).

Author contributions S.P. and K.S. conceived the project. S.P., R.P. and B.V. performed the experiments, with assistance from H.F.O. J.D.W. performed the modelling, with input from J.F., S.P. and K.S. S.P., R.P., B.V., J.D.W., J.F. and K.S. analysed data and wrote the paper.
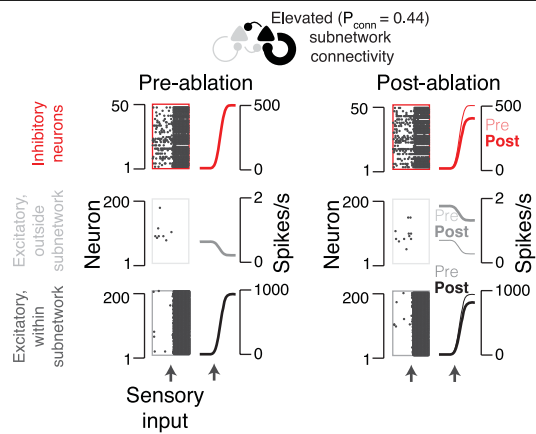
Extended Data Fig. 1 | Effect of ablation in a simulated network with hyper-connectivity (that is, $P_{conn} > 0.4$; here, $P_{conn} = 0.44$). Model network responses aligned to input (arrow, bottom). Raster plots show a subset of neurons from an example network. PSTHs show averages across all neurons and networks. Bottom, excitatory neurons within subnetwork. Middle, excitatory neurons outside subnetwork. Top, inhibitory neurons. Left, network response before ablation of 10% of the subnetwork neurons; right, response after ablation.
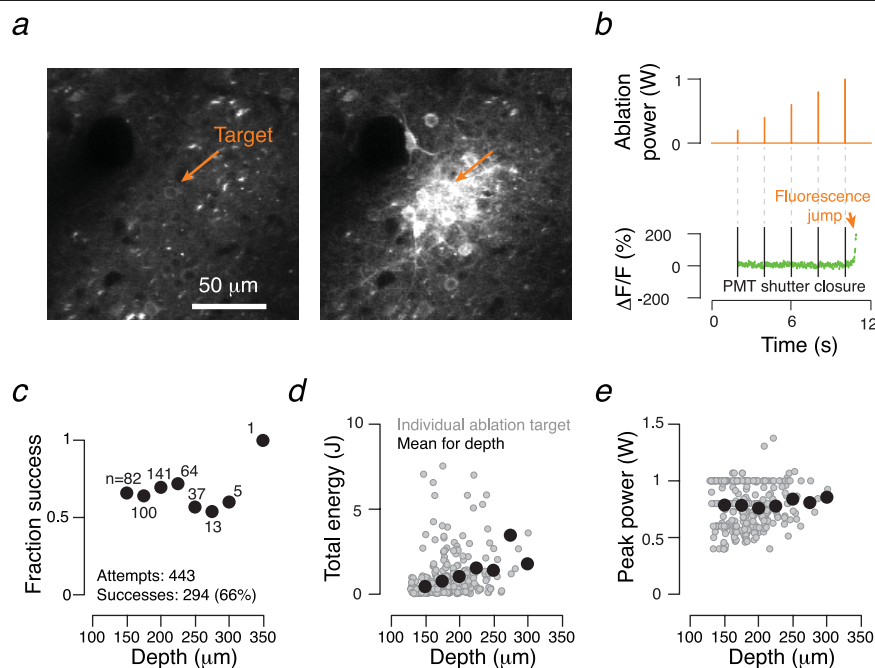
Extended Data Fig. 2 | Multi-photon ablation protocol. a, Example field of view immediately before (left) and after (right) ablation. Orange arrow denotes target neuron. **b**, Ablation protocol. Power (orange, top trace) during ablation epochs (100 ms; increased power, orange, top) gradually increased, and the PMT shutter was closed (black bars). During the intervening evaluation epochs, power was lower and constant (orange, top), and the PMT shutter was open. Ablation was terminated when GCaMP fluorescence at the target neuron (green) jumped (orange arrow). **c**, Success of ablation as a function of neuron depth for all experiments included in this dataset. Individual points give mean success rate for given depth bin; bin size, 25 μm. **d**, Depth dependence of total energy deposition for successful ablations (successfully ablated cells only: n = 293 cells across 22 sessions, 14 mice; ablations from j250220 and j257218, along with 7 additional ablations from other mice were excluded owing to incomplete logging). Grey dots denote individual ablations. Black dots, means across 25-μm bins. **e**, As in **d**, but for peak power needed for ablation (n = 293 cells across 22 sessions, 14 mice).
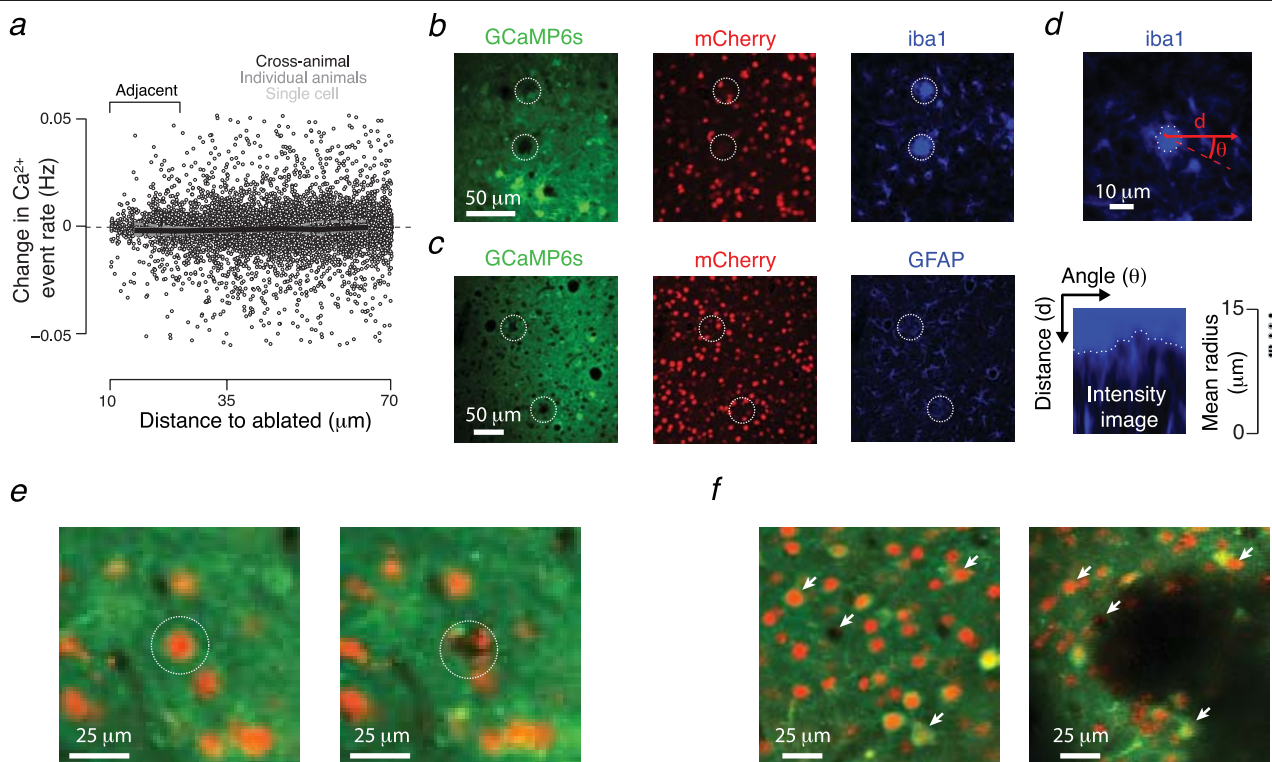
Extended Data Fig. 3 | Multi-photon ablation produces spatially localized effects. a, Change in calcium event rate (Methods) as a function of minimal distance to an ablated neuron after silent cell ablation. Individual neurons appear as grey points, with dark grey dashed lines showing single mouse averages and the dark black line showing the cross-mouse ($n = 8$ silent ablation mice) average. Event rates among neurons adjacent to ablated silent cells did not change (event rate before ablation: 0.014 ± 0.008 Hz, grand median $\pm$ adjusted MAD; after ablation: 0.014 ± 0.007 Hz; $P = 0.055$ before versus after ablation, Wilcoxon signed-rank test, paired medians across $n = 8$ mice; 1,028 neurons across all mice) (Methods). **b**, Confocal ex vivo image from a mouse perfused 24 h after ablation. Ablation sites are indicated with dashed white circles. Green, GCaMP6s fluorescence; red, mCherry fluorescence; blue, microglial antibody IBA1 fluorescence. **c**, As in **b**, but blue shows immunoreactivity for the astrocytic marker GFAP. **d**, The spatial extent of glial reaction was measured by detecting the fastest intensity decline ridge (dashed white line) in the glial antibody image along lines emanating from the ablation centre at varied angles (Methods). Top, ridge along ablation from **b**. Bottom left, intensity image in angle-distance space within which the ridge was measured. Bottom right, distribution of reaction radii; all points constitute IBA1 labelling, as no detectable glial reactions were observed with GFAP: 8 out of 10 IBA1-labelled and 0 out of 6 GFAP-labelled ablations retrieved histologically revealed a detectable glial reaction (Methods). These reactions had radii of 11.7 ± 1.7 µm (mean $\pm$ s.d.; $n = 8$ sites). **e**, Two-photon in vivo images before (left) and after (right) a successful ablation (target, white dotted line). Green, GCaMP6s fluorescence; red, mCherry fluorescence. **f**, As in **e**, but after a failure of the ablation protocol to terminate the ablation. Excess energy deposition produced a large lesion (black, centre of image). White arrows denote corresponding points in the two images. Mice ($n = 5$) with such lesions were excluded from the study.
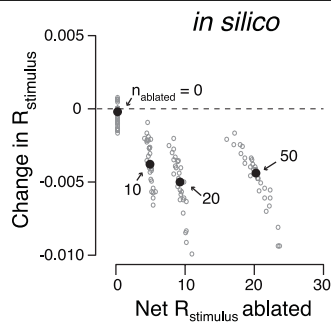
Extended Data Fig. 4 | Effect of ablation on L2/3 model sensory representation increases with the number of ablated neurons. Ablation effect (change in $R_{stimulus}$) as a function of the degree of touch representation degradation (net $R_{stimulus}$ across ablated neurons). In all cases, we used increased subnetwork connectivity (0.4) (Fig. 1, Methods). The $n_{ablated}$ neurons with the highest encoding score were selected for ablation. Grey circles denote individual networks. Black dots denote, median across $n = 30$ simulated networks for a given number of ablated neurons, indicated in the plot. Beyond $n_{ablated} > 50$, we observed instability, presumably because we did not attempt to restore excitatory-inhibitory balance after ablation; these data were omitted. Correlation of net $R_{stimulus}$ ablated and $\Delta R_{stimulus}$: $R = -0.65$, $P < 0.01$.
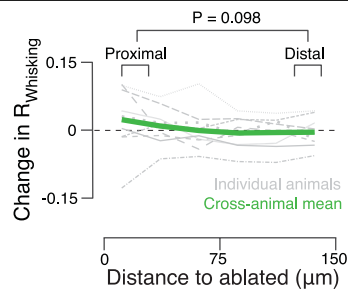
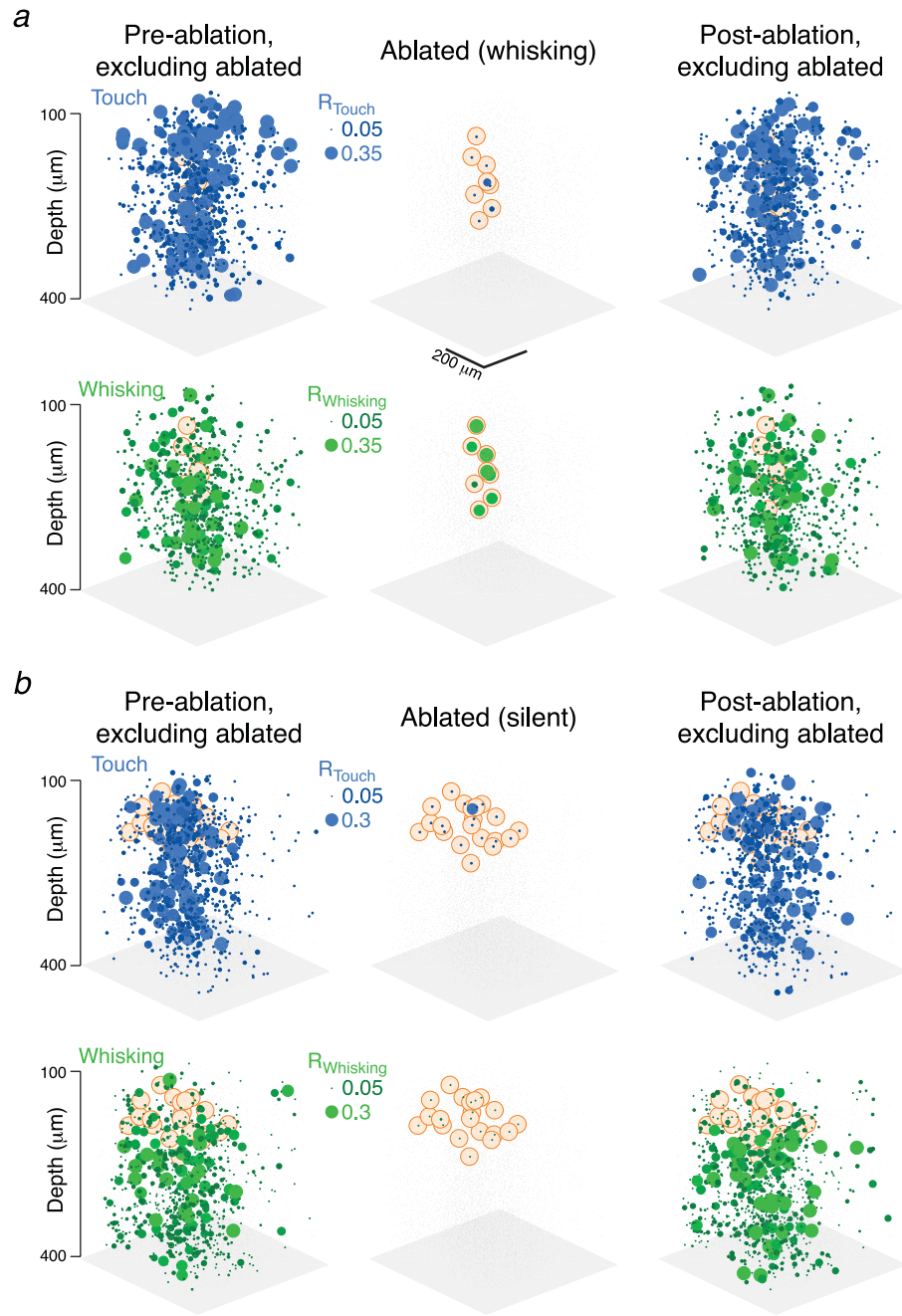**Extended Data Fig. 5 | Ablation of touch neurons does not produce distance-dependent effects in the whisking representation.** Proximal (15–35 µm to nearest ablated cell) change in $P_{whisking}$: 0.000 ± 0.192 (grand median ± adjusted MAD); distal (115–135 µm): −0.023 ± 0.186. P value given for Wilcoxon signed-rank test comparing proximal paired to distal (n = 9 mice). Legend as in Fig. 2m.
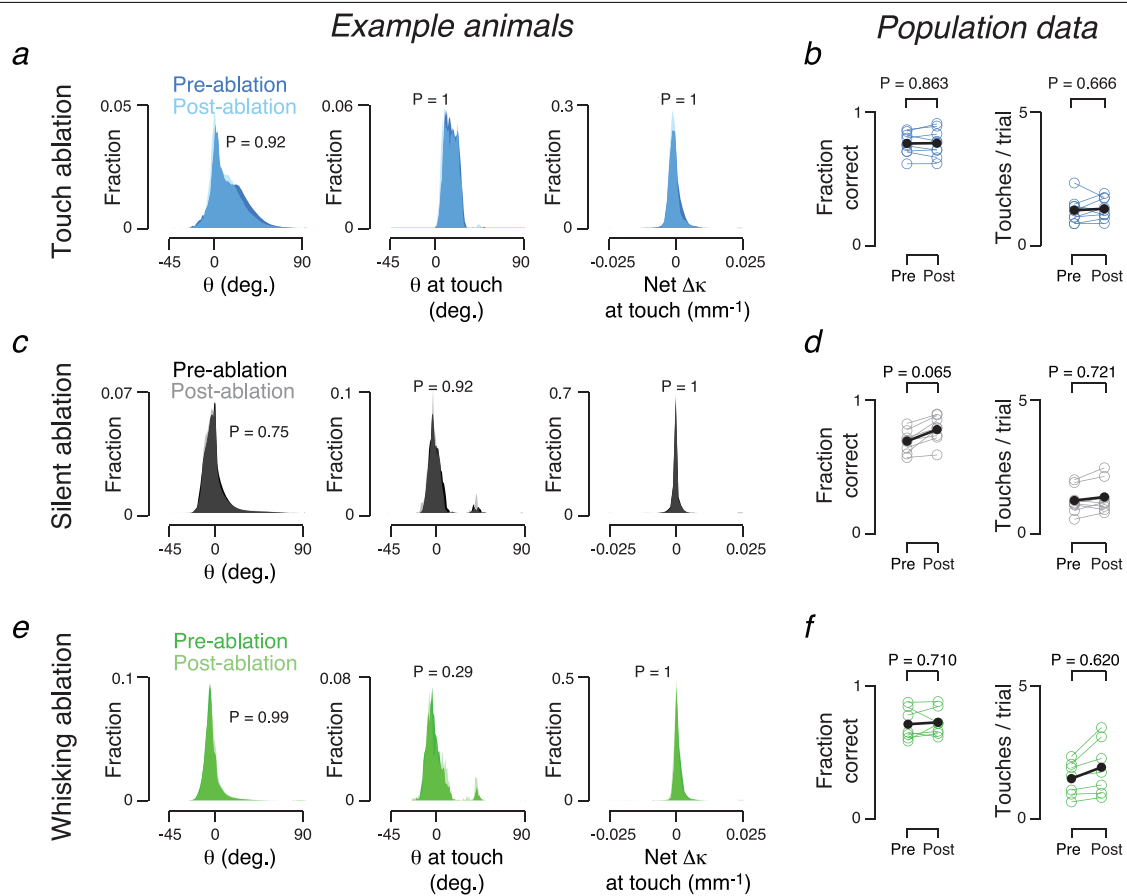
**Extended Data Fig. 6 | Behaviour does not account for ablation effects.**
a, Pre-touch (dark blue) and post-touch (light blue) distributions of neuron ablation for whisker angle (θ), angle at touch (θ at touch), and net curvature change across all touches (net Δκ at touch) in an example mouse. *P* values from a Kolmogorov–Smirnov test comparing the distribution of a variable before and after ablation in individual mice. No mice showed a significant (*P* < 0.05) change in any of the three parameters. **b**, Fraction of correct trials (left) and number of touches (right) before and after ablation of touch neurons. *P* values from a Wilcoxon signed-rank test, paired by mouse (*n* = 9 mice). **c**, **d**, As in **a** and **b**, but for ablations of silent neurons (*n* = 8 mice). **e**, **f**, As in **a** and **b**, but for ablations of whisking neurons (*n* = 7 mice).

Extended Data Fig. 7 | Example effects of ablations of whisking and silent neurons. a, Example ablation of a whisking neuron. Left, example maps for touch (top, blue) and whisking (bottom, green) cells before ablation. Sphere size corresponds to R_{touch} (top) or $R_{whisking}$ (bottom) values. Grey dots denote other neurons. These maps exclude the ablated neurons, the position of which is indicated by a faint orange background. Centre, R_{touch} (top) and $R_{whisking}$ (bottom) values for the ablated population. Right, R_{touch} (top) and $R_{whisking}$ (bottom) values after ablation, with ablated neurons again excluded. **b**, As in **a**, but for ablation of silent neurons.
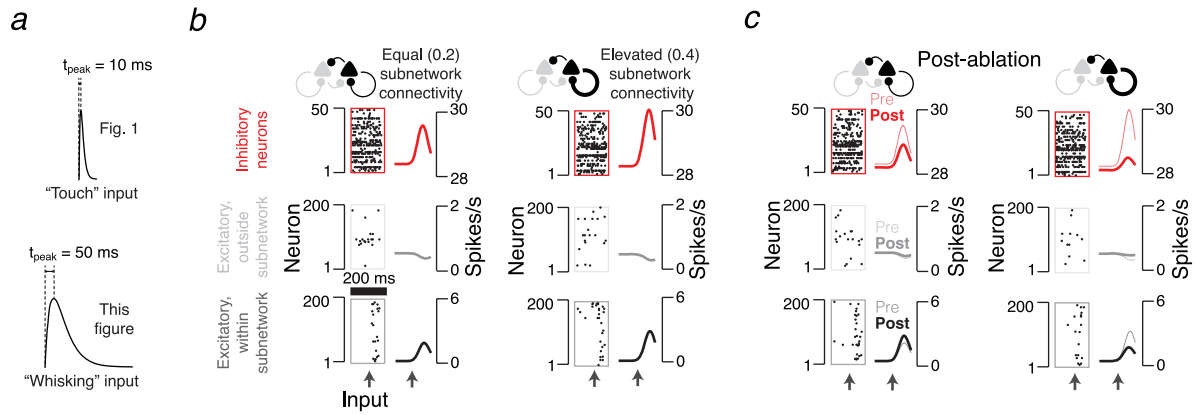
Extended Data Fig. 8 | Simulation of ablation of whisking neurons produces representation degradation in networks with increased, but not equal subnetwork connectivity. a, Whisking input was simulated by using input with a peak time of 50 ms (bottom), in contrast to 10 ms for touch (top) (Fig. 1). **b**, Model network responses aligned to input before ablation. Left to right, increasing subnetwork connectivity. Bottom to top, raster plots (each showing a subset of neurons from an example network) and PSTHs (averaged across all neurons and networks) for the three neuronal populations in the model (Fig. 1a, Methods). **c**, As in **b**, but after ablation. Thin PSTHs are before ablation. Change in encoding score after ablation: from 0.143 ± 0.024 to 0.104 ± 0.013, grand median ± adjusted MAD. $P < 0.001$, Wilcoxon signed-rank test paired by network ($n = 30$ networks).

Extended Data Table 1 | Individual mice are listed with the number of neurons imaged, the type(s) of ablation(s) performed, and the number of neurons ablated

Animal ID	Cell count	Ablated type	Ablated count	Touch count	ΔR_{touch}	Whisking count	$\Delta R_{whisking}$
j250220	8,844	touch	50	867	-0.122	422	-0.076
j257218	6,215	silent	20	743	0.018	366	0.032
j257220	3,663	touch	9	389	-0.004	455	0.025
j258836	7,290	silent	16	481	0.066	666	-0.012
		touch	15	488	-0.055	655	0.001
j271211	9,415	silent	16	2,476	-0.012	551	-0.007
		touch	15	1,951	-0.061	692	0.021
j278937	4,230	silent	15	146	0.004	379	0.001
		whisking	12	150	-0.006	392	0.011
j278939	7,167	silent	20	636	-0.024	698	0.001
		whisking	13	523	-0.017	649	-0.015
j281915	7,002	whisking	8	723	-0.010	550	0.004
		touch	11	601	-0.022	672	0.008
n274424	7,785	touch	17	706	-0.029	718	-0.014
n272761	6,359	touch	14	509	-0.001	410	0.000
n274577	12,173	touch	11	1,380	-0.013	657	0.004
n275801	8,354	silent	14	220	0.000	738	-0.007
		touch	9	197	-0.065	698	-0.006
n275798	11,364	silent	13	959	0.002	958	0.002
		whisking	11	972	0.008	1,037	0.011
n278288	9,314	whisking	25	969	-0.008	813	-0.006
n276013	11,659	silent	16	652	0.028	1,072	-0.001
		whisking	9	634	-0.012	968	-0.008
n278759	9,187	whisking	11	617	-0.003	526	-0.004

The number of touch and whisking neurons is given (for the 0.1 encoding score criteria) (Methods), as well as the change in median encoding score after ablation. Mice with IDs starting with a 'j' were virally transfected *Emx1-cre × LSL-H2B-mCherry*[7]; mice with IDs starting with an 'n' were *Ai162 × Slc17a7-IRES-cre*[40].

Corresponding author(s):   Simon Peron

Last updated by author(s):   Dec 22, 2019

Reporting Summary

Nature Research wishes to improve the reproducibility of the work that we publish. This form provides structure for consistency and transparency in reporting. For further information on Nature Research policies, see Authors & Referees and the Editorial Policy Checklist.

Statistics

For all statistical analyses, confirm that the following items are present in the figure legend, table legend, main text, or Methods section.

n/a	Confirmed	
☐	☒	The exact sample size (n) for each experimental group/condition, given as a discrete number and unit of measurement
☐	☒	A statement on whether measurements were taken from distinct samples or whether the same sample was measured repeatedly
☐	☒	The statistical test(s) used AND whether they are one- or two-sided *Only common tests should be described solely by name; describe more complex techniques in the Methods section.*
☐	☒	A description of all covariates tested
☐	☒	A description of any assumptions or corrections, such as tests of normality and adjustment for multiple comparisons
☐	☒	A full description of the statistical parameters including central tendency (e.g. means) or other basic estimates (e.g. regression coefficient) AND variation (e.g. standard deviation) or associated estimates of uncertainty (e.g. confidence intervals)
☐	☒	For null hypothesis testing, the test statistic (e.g. F, t, r) with confidence intervals, effect sizes, degrees of freedom and P value noted *Give P values as exact values whenever suitable.*
☒	☐	For Bayesian analysis, information on the choice of priors and Markov chain Monte Carlo settings
☒	☐	For hierarchical and complex designs, identification of the appropriate level for tests and full reporting of outcomes
☒	☐	Estimates of effect sizes (e.g. Cohen's d, Pearson's r), indicating how they were calculated

Our web collection on statistics for biologists contains articles on many of the points above.

Software and code

Policy information about availability of computer code

Data collection	Scanimage was used to collect imaging data. Norpix, along with custom MATLAB code was used for videography data collection. Behavior control and data collection was via BPod and custom MATLAB code.
Data analysis	Data analysis was performed with custom MATLAB code.

For manuscripts utilizing custom algorithms or software that are central to the research but not yet described in published literature, software must be made available to editors/reviewers. We strongly encourage code deposition in a community repository (e.g. GitHub). See the Nature Research guidelines for submitting code & software for further information.

Data

Policy information about availability of data

All manuscripts must include a data availability statement. This statement should provide the following information, where applicable:

- Accession codes, unique identifiers, or web links for publicly available datasets
- A list of figures that have associated raw data
- A description of any restrictions on data availability

Data are available at crcns.org.

Field-specific reporting

Please select the one below that is the best fit for your research. If you are not sure, read the appropriate sections before making your selection.

☒ Life sciences   ☐ Behavioural & social sciences   ☐ Ecological, evolutionary & environmental sciences

Life sciences study design

All studies must disclose on these points even when the disclosure is negative.

Sample size	Samples sizes were selected based on typical sample sizes in the field. 7-9 mice were used per ablation type. No statistical tests were used to determine sample size.
Data exclusions	Animals with excessive damage were excluded. Furthermore, neurons immediately adjacent to the ablated cells were excluded from analysis. These criteria were determined prior to experiments, and are described in detail in the manuscript.
Replication	We did 7-9 replications of each experiment. All presented results were reproducible across replicates.
Randomization	Mice were assigned randomly to experimental groups (ablation type).
Blinding	Experimenters were not blind to the group each mouse belonged to.

Reporting for specific materials, systems and methods

We require information from authors about some types of materials, experimental systems and methods used in many studies. Here, indicate whether each material, system or method listed is relevant to your study. If you are not sure if a list item applies to your research, read the appropriate section before selecting a response.

Materials & experimental systems

n/a	Involved in the study
☐	☒ Antibodies
☒	☐ Eukaryotic cell lines
☒	☐ Palaeontology
☐	☒ Animals and other organisms
☒	☐ Human research participants
☒	☐ Clinical data

Methods

n/a	Involved in the study
☒	☐ ChIP-seq
☒	☐ Flow cytometry
☒	☐ MRI-based neuroimaging

Antibodies

Antibodies used	We used antibodies for microglial marker iba1 (Abcam, ab5076) or the astrocytic marker GFAP (Abcam, ab7260).
Validation	Validation was implicit. Microglia and astrocytes typically have uniform reactivity in cortex. We looked for, and observed, this pattern in tissue that was not subject to ablation.

Animals and other organisms

Policy information about studies involving animals; ARRIVE guidelines recommended for reporting animal research

Laboratory animals	Transgenic mice are listed in the table, Extended Data Table 1. We used two types of mice: a cross between R26-LSL-H2B-mCherry (JAX 023139) and exm1-Cre (JAX 005628), as well as crosses of Ai162 (JAX 031562) and Slc17a7-IRES2-Cre (JAX 023527).
Wild animals	N/A
Field-collected samples	N/A
Ethics oversight	All procedures were performed in compliance with the Janelia Research Campus Institutional Animal Care and Use Committee and the New York University University Animal Welfare Committee.

Note that full information on the approval of the study protocol must also be provided in the manuscript.